material, ICF-22 InS-Li (Supplementary Information). Its specific conductivity reaches up to 1.1×10^{-2} ohm^{-1} cm^{-1} at 24 °C under 31.7% relative humidity (Fig. 5). The ionic conductivity of these chalcogenides generally increases with the relative humidity. For example, at 18 °C, the conductivity of ICF-5 CuInS-Na ranges from 1.0×10^{-4} ohm^{-1} cm^{-1} under 0.2% relative humidity to 1.2×10^{-2} ohm^{-1} cm^{-1} under 100% relative humidity (Fig. 3a, b). A similar trend is observed for ICF-21 InSe-Na (Fig. 4a, b).

Despite their high ionic conductivity, there are some limitations for the practical applications of these materials, particularly for lithium batteries, because a relative humidity of 30% or higher is needed to achieve the highest ionic conductivity. Another possible application might take advantage of the open architecture and narrow bandgaps (as compared to oxides) of these materials for photocatalysis. In either case, further research is needed to develop these materials for practical applications.

The materials reported are probably only a small group of a much larger family of inorganic open-framework chalcogenides. The synthetic method described here should be applicable to a range of chalcogenide structures and compositions. The diverse chemical compositions and crystal structures provide rich opportunities in exploring the physical and chemical properties of these chalcogenides and in establishing structure–property relationships. □

Methods

Typical synthesis conditions are given below using ICF-22 InS-Li, ICF-21 InSe-Na, and ICF-5 CuInS-Na as examples.

For ICF-22 InS-Li, $In(NO_3)_3{\cdot}H_2O$ (339.2 mg), LiCl (176.9 mg), Li_2S (210.3 mg), and H_2O (2.1967 g) were mixed and stirred in a 23-ml Teflon-lined stainless steel autoclave for 20 min. The vessel was then sealed and heated at 190 °C for 4 days. After cooling to room temperature, a ~68% yield of colourless crystals was obtained.

For ICF-21 InSe-Na, a mixture of $In(NO_3)_3{\cdot}H_2O$ (381.5 mg), Na_2Se (408.3 mg), and H_2O (2.0240 g) was prepared and stirred in a 23-ml Teflon-lined stainless steel autoclave for 10 min. The vessel was then sealed and heated at 170 °C for 3 days. The autoclave was cooled to room temperature. A ~77% yield of pale-yellow octahedral crystals was obtained.

For ICF-5 CuInS-Na, $In(NO_3)_3{\cdot}H_2O$ (372.0 mg), $Cu(NO_3)_2{\cdot}3H_2O$ (67.98 mg), Na_2S (234.4 mg), and water (2.5740 g) were mixed in a 23-ml Teflon-lined stainless steel autoclave and stirred for 10 min. The vessel was then sealed and heated at 150 °C for 3 days. After cooling to room temperature, a ~85% yield of red crystals was obtained.

For ICF-5 CuInS-Na, the elemental analysis (wt%) was 44.22 In, 4.03 Cu (calculated 43.97 In, 4.29 Cu) based on the formula $Na_{10}[Cu_3In_{17}S_{33}]{\cdot}56(H_2O)$. The thermal analysis shows that ICF-5 CuInS-Na undergoes a total of 17.0% water loss in the temperature range from room temperature to 200 °C. All crystal structures were solved from single crystal data collected at 150 K on a SMART 1000 charge-coupled device (CCD) diffractometer.

Ionic conductivities were measured by a.c. impedance methods with an applied frequency range of 10 to 20 MHz using a Solartron 1260 frequency response analyser. Both pellet and single crystal samples were used for measurements. Pellets were prepared by compressing the fresh powder sample at the pressure of 5,000 psi and were then cut into smaller pellets shaped like the rectangular prism. Liquid gallium was used as contacting electrodes.

Received 4 May; accepted 27 October 2003; doi:10.1038/nature02159.

1. Flanigen, E. M. in *Introduction to Zeolite Science and Practice* (eds van Bekkum, H., Flanigen, E. M. & Jansen, J. C.) 13–34 (Elsevier, New York, 1991).
2. Breck, D. W. *Zeolite Molecular Sieves, Structure, Chemistry, and Use* (John Wiley & Sons, New York, 1974).
3. Davis, M. E. Ordered porous materials for emerging applications. *Nature* **417,** 813 (2002).
4. Feng, P., Bu, X. & Stucky, G. D. Hydrothermal syntheses and structural characterization of zeolite analogue compounds based on cobalt phosphate. *Nature* **388,** 735–741 (1997).
5. Scott, R. W. J., MacLachlan, M. J. & Ozin, G. A. Synthesis of metal sulfide materials with controlled architecture. *Curr. Opin. Solid State Mater. Sci.* **4,** 113–121 (1999).
6. Huo, Q., Leon, R., Petroff, P. M. & Stucky, G. D. Mesostructure design with gemini surfactants: supercage formation in a three-dimensional hexagonal array. *Science* **68,** 1324–1327 (1995).
7. Zhao, D. *et al.* Triblock copolymer syntheses of mesoporous silica with periodic 50 to 300 angstrom pores. *Science* **279,** 548–552 (1998).
8. Johnson, S. A., Ollivier, P. J. & Mallouk, T. E. Ordered mesoporous polymers of tunable pore size from colloidal silica templates. *Science* **283,** 963–965 (1999).
9. Cheetham, A. K., Ferey, G. & Loiseau, T. Open-framework inorganic materials. *Angew. Chem. Int. Edn* **38,** 3268–3292 (1999).
10. West, A. R. *Solid State Chemistry and its Applications* (Wiley, New York, 1992).
11. Zheng, N., Bu, X. & Feng, P. Microporous and photoluminescent chalcogenide zeolite analogs. *Science* **298,** 2366–2369 (2002).
12. Bedard, R. L., Wilson, S. T., Vail, L. D., Bennett, J. M. & Flanigen, E. M. in *Zeolites: Facts, Figures, Future. Proc. 8th Int. Zeolite Conf.* (eds Jacobs, P. A. & van Santen, R. A.) 375 (Elsevier, Amsterdam, 1989).
13. Cahill, C. L. & Parise, J. B. On the formation of framework indium sulfides. *J. Chem. Soc. Dalton Trans.* 1475–1482 (2000).
14. Dhingra, S. & Kanatzidis, M. G. Open framework structures based on Se_x^{2-} fragments: synthesis of $(Ph_4P)[M(Se_6)_2]$ (M = Ga, In, Tl) in molten $(Ph_4P)_2Se_x$. *Science* **258,** 1769–1772 (1992).
15. Li, H., Laine, A., O'Keeffe, M. & Yaghi, O. M. Supertetrahedral sulfide crystals with giant cavities and channels. *Science* **283,** 1145–1147 (1999).
16. Wehmschulte, R. J. & Power, P. P. Low-temperature synthesis of aluminum sulfide as the solvate $Al_2S_6(NMe_3)_4$ in hydrocarbon solution. *J. Am. Chem. Soc.* **119,** 9566–9567 (1997).
17. Bu, X., Zheng, N., Li, Y. & Feng, P. Pushing up the size limit of chalcogenide supertetrahedral clusters: two- and three-dimensional photoluminescent open frameworks from $(Cu_5In_{30}S_{54})^{13-}$ clusters. *J. Am. Chem. Soc.* **124,** 12646–12647 (2002).
18. Hoppe, R., Lidecke, W. & Frotath, F. C. Sodium thioindate and sodium selenoindate. *Z. Anorg. Allgem. Chem.* **309,** 49–54 (1961).

Supplementary Information accompanies the paper on **www.nature.com/nature**.

Acknowledgements We acknowledge the support of this work by the NSF. We also thank Y. Yan and his group for assistance with impedance measurements.

Competing interests statement The authors declare that they have no competing financial interests.

Correspondence and requests for materials should be addressed to P. F. (pingyun.feng@ucr.edu).

Explosive volcanism may not be an inevitable consequence of magma fragmentation

Helge M. Gonnermann & Michael Manga

Earth and Planetary Science, University of California, Berkeley, California 94720, USA

The fragmentation of magma, containing abundant gas bubbles, is thought to be the defining characteristic of explosive eruptions[1–3]. When viscous stresses associated with the growth of bubbles and the flow of the ascending magma exceed the strength of the melt[2,4–6], the magma breaks into disconnected fragments suspended within an expanding gas phase. Although repeated effusive and explosive eruptions for individual volcanoes are common[7,8], the dynamics governing the transition between explosive and effusive eruptions remain unclear. Magmas for both types of eruptions originate from sources with similar volatile content, yet effusive lavas erupt considerably more degassed than their explosive counterparts[7,8]. One mechanism for degassing during magma ascent, consistent with observations, is the generation of intermittent permeable fracture networks generated by non-explosive fragmentation near the conduit walls[9–11]. Here we show that such fragmentation can occur by viscous shear in both effusive and explosive eruptions. Moreover, we suggest that such fragmentation may be important for magma degassing and the inhibition of explosive behaviour. This implies that, contrary to conventional views, explosive volcanism is not an inevitable consequence of magma fragmentation.

Analysis of pumice samples from the explosive eruption of Mount Pinatubo, 15 June 1991, suggests that non-newtonian rheology and growth of gas bubbles during magma ascent led to intense shear and possibly fragmentation at the conduit walls[9]. Recent observations suggest that fragmentation at the conduit walls may not be restricted to explosive eruptions. Tuffen *et al.*[10] describe multiple generations of tuffisite veins in the dissected vent of a rhyolite lava flow at Torfajökull, Iceland. They[10] interpret these features to record repeated cycles of brittle fragmentation followed by annealing of the fragments and subsequent deformation of the reannealed magma by viscous flow, to form flow banding. Textures within the tuffisite veins suggest that fragmentation created a

transient fracture system amenable to gas flow. Similar examples of apparent fragmentation, reannealing and deformation of fragments into flow banding are also observed in the Mule Creek vent, New Mexico[11]. Non-explosive fragmentation of ascending magma has also been suggested for the generation of volcanic earthquakes during the 1991–1995 effusive eruption of the Unzen volcano, Japan[12]. We have examined obsidians from the Big Glass Mountain rhyolite dome, California, and find corroborating evidence of magma fragmentation, reannealing and elongation of fragments into flow banding (Fig. 1).

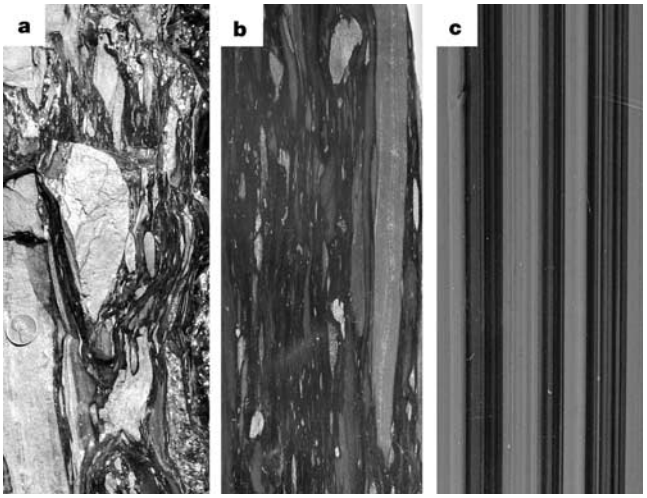

Figure 1 Deformation textures of annealed fragments in obsidian from Big Glass Mountain, California. **a**, Annealed fragments are slightly elongate parallel to shear direction; sample width is 11.5 cm. **b**, Annealed and deformed fragments; sample width is 6 cm. **c**, Typical 'flow banding'; sample width is 4 cm. Fragment compositions in all three samples are identical: the difference in colour is primarily due to varying abundance of micrometre-size crystals.

To gain insight into the mechanics governing fragmentation in silicic volcanoes, we have developed a numerical model for magma ascent in the volcanic conduit. The ascending magma (that is, melt + bubbles) is modelled as the steady, isothermal flow of a single-phase liquid at constant mass flux, Q_m, in a cylindrical conduit of constant radius R. We specify a magma pressure, $p_m = p_0$, number density of bubbles, n_d, and relaxed newtonian melt viscosity, μ_{mr}, at the base of the conduit to solve the joint problem of bubble growth and magma ascent. Rather than include the transition to fragmentation and flow of fragmented magma, we determine the ascent distance above the conduit entry at which magma fragmentation by viscous shear should first occur. Unlike previous studies[3,13], the model is quasi-one-dimensional and for a given depth computes the radially varying vertical component of magma velocity, $u(r,z)$. Mass and momentum equations solved by our model are:

$$\frac{\mathrm{d}}{\mathrm{d}z}\left[\rho(z)\int_A u(r,z)\ \mathrm{d}A\right] = \frac{\mathrm{d}}{\mathrm{d}z}[\rho(z)\ Q(z)] = \frac{\mathrm{d}}{\mathrm{d}z}Q_m = 0 \qquad (1)$$

and

$$\mu(\dot{\gamma},\phi,c,a,r,z)\ \dot{\gamma}(r,z) = -\frac{r}{2}\ \frac{\mathrm{d}p(z)}{\mathrm{d}z} \qquad (2)$$

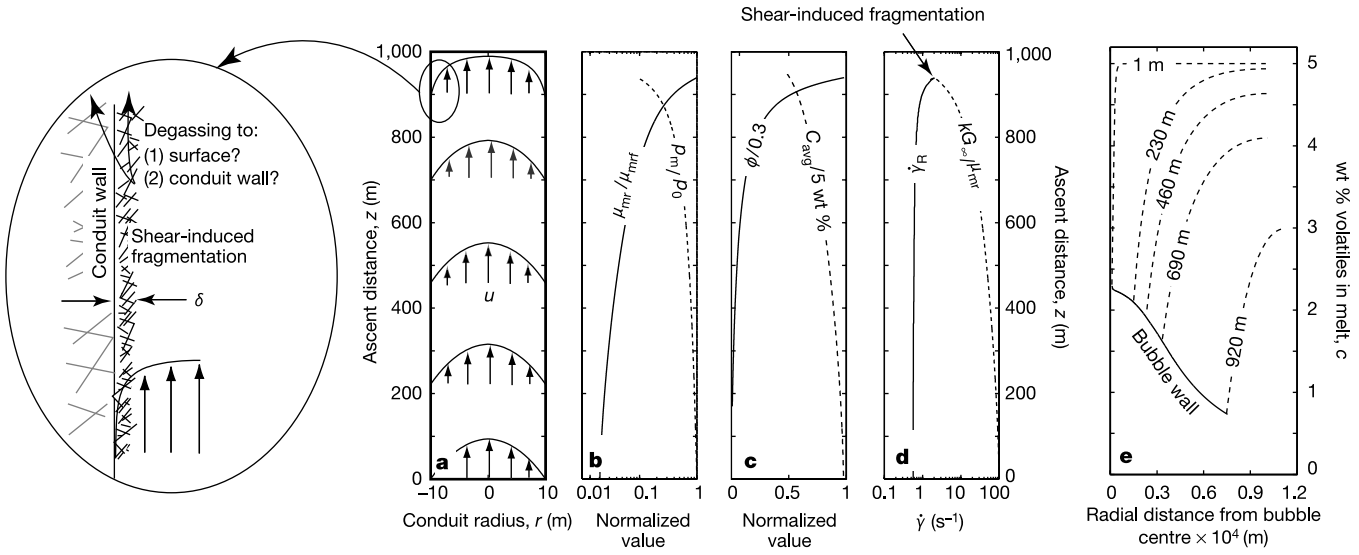

Figure 2 Evolution of a typical model simulation. The model simulation starts at an ambient pressure of 250 MPa and ends once shear-induced fragmentation is first predicted to occur. **a**, Calculated velocity profiles, $u(r)$, of the ascending magma, shown at different ascent distances. The inset is a schematic depiction of the theoretical model for shear-induced magma fragmentation near the conduit walls and concurrent open-system degassing. Small hatch marks schematically indicate shear-induced fragmentation, which for this model calculation is inferred to occur at 920 m. The presence of shear-induced fragmentation above the initial fragmentation level is hypothetical and is not based on actual model calculations. The two large arrows indicate possible degassing pathways associated with the increased permeability of fragmented magma. **b**, Relaxed melt viscosity normalized by its value at the first occurrence of shear-induced fragmentation (μ_{mr}/μ_{mrf}, solid line) and ambient pressure normalized by its value at zero ascent distance (p_m/p_0, dashed line) versus ascent distance. The gradient in p_m is the sum of magma-static and dynamic pressure changes. **c**, Normalized magma vesicularity (solid line) and normalized volumetrically averaged dissolved volatile content (dashed line) versus ascent distance. **d**, Calculated radial strain rate at the conduit wall ($\dot{\gamma}_R$, solid line) and critical strain rate for fragmentation (kG_∞/μ_{mr}, dashed line) versus ascent distance. The calculated values of $\dot{\gamma}_R$ increase with ascent distance as the velocity profile becomes increasingly blunt and the largest strain rates are near the conduit walls. The critical strain rate decreases as the relaxed melt viscosity increases with volatile exsolution. When calculated $\dot{\gamma}_R$ and critical strain rate are equal, the first occurrence of shear-induced fragmentation is inferred and the model calculation ends. **e**, Dissolved volatile content of the melt. Each concentration profile (dashed line) corresponds to one velocity profile shown in **a**. Also shown is the change in bubble radius and volatile content at the bubble wall (solid line). Diffusion of volatiles into the gas bubbles, as a consequence of decreasing p_m, results in decreasing volatile content of the melt and increasing μ_{mr} shown in **b**.

with boundary conditions:

$$u(R,z) = \frac{\mathrm{d}u(0,z)}{\mathrm{d}r} = 0 \quad (3)$$

Here A is the cross-sectional area of the conduit, $\rho(z)$ is the magma density, $Q(z) = Q_m/\rho(z)$ is the volumetric flow rate, $\mu(r,z)$ is the magma viscosity, $p(z)$ is the dynamic pressure, r and z are the radial and vertical coordinates respectively, $\dot{\gamma} = \mathrm{d}u/\mathrm{d}r$ is the rate of simple shear strain, $\phi(z)$ is magma vesicularity, $a(z)$ is bubble radius, and $c(z)$ is the concentration of volatiles dissolved in the melt. Calculations of volatile exsolution and bubble growth, which occur as a consequence of depressurization during magma ascent, assume a homogeneous suspension of spherical bubbles surrounded by uniform shells of silicate melt[14] with a volatile-dependent viscosity[15].

During the flow calculations, magma viscosity is allowed to vary vertically and radially. Locally, magma viscosity depends on melt viscosity, μ_m, and strain-rate dependent suspension (melt + bubbles) rheology[16–18]. Melt viscosity, in turn, depends on strain rate[4–6,19], as well as volatile content[20]. We do not explicitly model the growth of crystals during magma ascent. However, the effect of crystallinity on magma rheology can be represented by increased magma viscosity[21], in accordance with rheological models for suspensions of rigid particles[16–18].

Figure 2 depicts the typical changes in flow conditions and radial velocity profiles (Fig. 2a) calculated by our model. During ascent, magma pressure decreases from its initial value through magmastatic and dynamic pressure loss (Fig. 2b) as:

$$p_m = p_0 - \int_0^z \left[\frac{\mathrm{d}p}{\mathrm{d}z} + g\rho(z)\right] \mathrm{d}z \quad (4)$$

This results in volatile exsolution and bubble growth[14,15] (Fig. 2e), which in turn causes ϕ, Q, and μ_{mr} to increase (Fig. 2b,c). Because of the rheological dependence on $\dot{\gamma}$, there is an inherent feedback between increasing $\dot{\gamma}$ and decreasing μ. The no-slip boundary condition results in large shear–strain rates at the conduit walls, $\dot{\gamma} = \dot{\gamma}_R$, and the initially near-newtonian velocity profile of the ascending magma becomes increasingly blunt[18] (Fig. 2a).

The melt closest to the conduit walls will eventually be subjected to shear–strain rates that exceed the experimentally determined critical strain rate of silicate melts[2,4,12] (Fig. 2d). In our simulations, the Capillary number, $\mathrm{Ca} = \mu_m\dot{\gamma}_R a/\sigma$, is $\gg 1$ near the conduit walls, and we can assume that strain rates of magma and melt are similar[21]. Here σ is surface tension. We adopt a criterion for magma fragmentation:

$$\dot{\gamma} \geq \kappa\frac{G_\infty}{\mu_{mr}} \quad (5)$$

where $\kappa = 0.01$ is an experimental constant and $G_\infty = 10$ GPa is the elastic modulus at infinite frequency.

At the threshold for 'shear-induced fragmentation', the melt surrounding gas bubbles is assumed to break by brittle failure[2–6]. Therefore, we expect that fragmentation depends primarily on the rheology of the melt phase, rather than the magma. We adopt a critical shear–strain rate that is based on the relaxed newtonian melt viscosity, a measured quantity during experimental determination of critical strain rates[4–6]. However, given the multiphase nature of natural magmas, the validity of either assumption requires future experimental evaluation[3].

From our model simulations we find that shear-induced fragmentation is predicted to occur over a wide range of parameters[22] encompassing explosive as well as effusive eruption conditions (Fig. 3). The evolution of individual model simulations follows the grey horizontal lines from low to high melt viscosity, until the fragmentation threshold, denoted by dots and squares, is reached (Fig. 3). Our results indicate that the threshold for shear-induced fragmentation follows a systematic trend (diagonal line on Fig. 3) that scales with the critical conduit shear–strain rate, $\dot{\Gamma} = Q/\pi R^3$, via the relaxed melt viscosity as:

$$\dot{\Gamma} \approx C\ G_\infty\ \mu_{mr}^{-0.9} \quad (6)$$

where $C = 0.01\ (\mathrm{Pa\,s})^{-0.1}$ is a fitting parameter. At a given Q and R, shear-induced fragmentation is predicted to occur once μ_{mr} exceeds the threshold value given by equation (6).

The degassed nature of effusive magmas is generally attributed to open system degassing[7,8,23], the loss of volatiles from the ascending magma. To what extent degassing is controlled by permeable gas flow laterally into the conduit wall[1,23], or vertically through the magma column[24], remains an open question. Permeability estimates[25–27] of $\leq 10^{-13}$ m^2 imply timescales of the order of weeks to years for permeable gas flow through vesicular magma within the conduit. However, based on recent observations[10,11] we speculate that shear-induced fragmentation may create, at least temporarily and locally, a magma consisting of individual fragments bound by an interconnected fracture network of high permeability. Degassing of centimetre-size fragments into fractures, concurrent with gas flow through a highly permeable fracture network, could considerably shorten the time required for degassing of magma at and above the initial depth of fragmentation. At the initial occurrence of fragmentation almost all deformation associated with magma ascent is localized over a radial distance, $\delta \approx CR\mu_{mr}^{0.1}$, derived by combining equations (5) and (6) under the assumption of conservation of mass. δ is an estimate for the thickness of fractured, and presumably permeable, magma that is expected to form during one cycle of shear-induced fragmentation. Therefore, regardless of the actual degassing pathway, shear-induced fragmentation may increase the feasibility of open-system degassing.

Observations[10] (Fig. 1) suggest that fragmented magma can

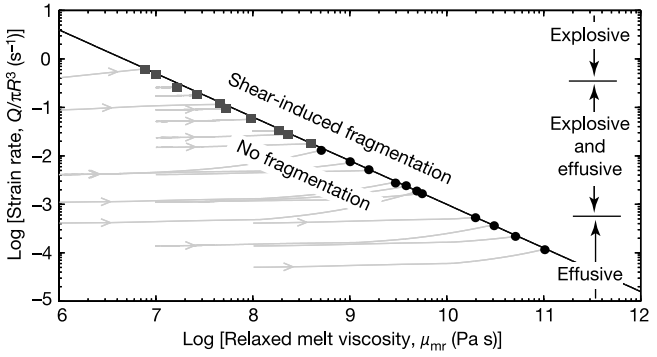

Figure 3 Model results and predicted occurrence of shear-induced fragmentation. Vertical axis is conduit strain rate (ratio of mean magma ascent velocity and conduit radius). Subhorizontal grey lines with arrows trace the evolution of conduit strain rate and μ_{mr} for individual model simulations. The predicted occurrence of shear-induced fragmentation is marked by symbols: circles, >70% of volatiles originally dissolved in the melt have exsolved at the time of shear-induced fragmentation; squares, an exsolved volatile fraction of <70%. The predicted occurrence of shear-induced fragmentation follows a systematic trend, well described by the power law of equation (6) (solid diagonal line). Below this trend no fragmentation is predicted to occur. A combination of conduit strain rate and μ_{mr} plotting above this trend is inferred to result in shear-induced fragmentation. Also shown are the ranges of explosive versus effusive strain rates for silicic eruptions, based on a compilation of eruption rates[22] and assuming an average magma density of approximately 10^3 kg m^{-3}, as well as a minimum (or maximum) conduit radius of the order of 10 m (or 100 m) for explosive (or effusive) eruptions. Our model simulations predict the occurrence of shear-induced fragmentation for both explosive and effusive eruption conditions. The following range of parameters were investigated: 100 MPa $\leq p_0 \leq$ 250 MPa, 10^{10} m$^{-3} \leq n_d \leq 10^{19}$ m^{-3}, 5 wt% $< c(z=0) <$ 8 wt%, $\phi(z=0) \approx 0$, 10^5 Pa s $\leq \mu_{mr}(z=0) \leq 10^8$ Pa s, 10^3 kg s$^{-1} \leq \int_A \rho(z)\, u(r,z)\, \mathrm{d}A < 10^9$ kg s^{-1}, and 5 m $\leq R \leq$ 200 m.

reanneal. Although our model simulations do not include calculations past the fragmentation threshold, we propose that a local decrease in shear-strain rates associated with fragmentation may promote reannealing[28]. Furthermore, it seems reasonable to assume that shear-induced fragmentation has a marked effect on the flow of the ascending magma and that upon continued ascent, fragments from different parts of the ascending magma may become juxtaposed. If the magma is texturally heterogeneous, which in itself may be a consequence of repeated cycles of fragmentation, flow deformation and reannealing, fragments can become elongated into bands[10] (Fig. 1). Minimum strain estimates to produce millimetre-size bands from decimetre-size fragments is of the order of 100. Using δ as an estimate of the length scale for shear, this corresponds to an ascent distance, $\Delta z \approx \dot{\gamma}_R \delta$, of the order of 10 m. We propose that the long-standing enigma of pervasive flow banding of silicic magmas may in some cases be viewed as a record of fragmentation and reannealing during magma ascent, in much the same way as banding can be made by fragmentation and reannealing in flows[29]. In addition, we expect that shear-induced fragmentation can, to some degree, replace viscous deformation as the mode of shear along conduit walls, thereby reducing the exceedingly large dynamic pressures required to erupt highly crystalline silicic magmas. However, none of our model simulations explicitly include the effect of crystals on fragmentation[30].

Our prediction that shear-induced fragmentation occurs in both explosive and effusive silicic volcanism is consistent with the observed conditions of volcanic systems[22] (Fig. 3), with the degassed nature of effusive silicic lavas[7,8], and with textural observations at the outcrop scale down to the microscale[9–11] (Fig. 1). As opposed to the common view that explosive volcanism "is defined as involving fragmentation of magma during ascent"[1], we conclude that fragmentation may play an equally important role in reducing the likelihood of explosive behaviour, by facilitating magma degassing. Because shear-induced fragmentation depends so strongly on the rheology of the ascending magma, our findings are in a broader sense equivalent to Eichelberger's hypothesis[1] that "higher viscosity of magma may favour non-explosive degassing rather than hinder it", albeit with the added complexity of shear-induced fragmentation. □

Received 19 May; accepted 15 November 2003; doi:10.1038/nature02138.

1. Eichelberger, J. C. Silicic volcanism: ascent of viscous magmas from crustal reservoirs. *Annu. Rev. Earth Planet. Sci.* **23,** 41–63 (1995).
2. Dingwell, D. B. Volcanic dilemma: Flow or blow? *Science* **273,** 1054–1055 (1996).
3. Papale, P. Strain-induced magma fragmentation in explosive eruptions. *Nature* **397,** 425–428 (1999).
4. Dingwell, D. B. & Webb, S. L. Structural relaxation in silicate melts and non-Newtonian melt rheology in geologic processes. *Phys. Chem. Miner.* **16,** 508–516 (1989).
5. Webb, S. L. & Dingwell, D. B. The onset of non-Newtonian rheology of silcate melts. *Phys. Chem. Miner.* **17,** 125–132 (1990).
6. Webb, S. L. & Dingwell, D. B. Non-Newtonian rheology of igneous melts at high stresses and strain rates: experimental results for rhyolite, andesite, basalt, and nephelinite. *J. Geophys. Res.* **95,** 15695–15701 (1990).
7. Newman, S., Epstein, S. & Stolper, E. Water, carbon dioxide and hydrogen isotopes in glasses from the ca. 1340 A.D. eruption of the Mono Craters, California: Constraints on degassing phenomena and initial volatile content. *J. Volcanol. Geotherm. Res.* **35,** 75–96 (1988).
8. Villemant, B. & Boudon, G. Transition from dome-forming to plinian eruptive styles controlled by H_2O and Cl degassing. *Nature* **392,** 65–69 (1998).
9. Polacci, M., Papale, P. & Rosi, M. Textural heterogeneities in pumices from the climactic eruption of Mount Pinatubo, 15 June 1991, and implications for magma ascent dynamics. *Bull. Volcanol.* **63,** 83–97 (2001).
10. Tuffen, H., Dingwell, D. B. & Pinkerton, H. Repeated fracture and healing of silicic magma generates flow banding and earthquakes? *Geology* **31,** 1089–1092 (2003).
11. Stasiuk, M. V. *et al.* Degassing during magma ascent in the Mule Creek vent (USA). *Bull. Volcanol.* **58,** 117–130 (1996).
12. Goto, A. A new model for volcanic earthquake at Unzen Volcano: Melt rupture model. *Geophys. Res. Lett.* **26,** 2541–2544 (1999).
13. Mastin, L. G. Insights into volcanic conduit flow from an open-source numerical model. *Geochem. Geophys. Geosyst.* **3,** doi:10.1029/2001GC000192 (2002).
14. Proussevitch, A. A., Sahagian, D. L. & Anderson, A. T. Dynamics of diffusive bubble growth in magmas: Isothermal case. *J. Geophys. Res.* **3,** 22283–22307 (1993).
15. Lensky, N. G., Lyakhovsky, V. & Navon, O. Radial variations of melt viscosity around growing bubbles and gas overpressure in vesiculating magmas. *Earth Planet. Sci. Lett.* **186,** 1–6 (2001).
16. Rust, A. C. & Manga, M. Effects of bubble deformation on the viscosity of dilute suspensions. *J. Non-Newtonian Fluid Mech.* **104,** 53–63 (2002).
17. Pal, R. Rheological behavior of bubble-bearing magmas. *Earth Planet. Sci. Lett.* **207,** 165–179 (2003).
18. Llewellin, E. W., Mader, H. M. & Wilson, S. D. R. The constitutive equation and flow dynamics of bubbly magmas. *Geophys. Res. Lett.* **29,** doi:10.1029/2002GL015697 (2002).
19. Simmons, J. H., Mohr, R. K. & Montrose, C. J. Non-Newtonian viscous flow in glass. *J. Appl. Phys.* **53,** 4075–4080 (1982).
20. Hess, K.-U. & Dingwell, D. B. Viscosities of hydrous leucogranitic melts: A non-Arrhenian model. *Am. Mineral.* **81,** 1297–1300 (1996).
21. Manga, M. & Loewenberg, M. Viscosity of magmas containing highly deformable bubbles. *J. Volcanol. Geotherm. Res.* **105,** 19–24 (2001).
22. Pyle, D. M. in *Encyclopedia of Volcanoes* (eds Sigurdsson, H., Houghton, B. F., McNutt, S. R., Rymer, H. & Stix, J.) 263–269 (Academic, San Diego, 2000).
23. Jaupart, C. & Allegre, C. J. Gas content, eruption rate and instabilities of eruption regime in silicic volcanoes. *Earth Planet. Sci. Lett.* **102,** 413–429 (1991).
24. Boudon, G., Villemant, B., Komorowski, J.-C., Ildefonse, P. & Semet, M. P. The hydrothermal system at Soufriere Hills volcano, Montserrat (West Indies): characterization and role in the on-going eruption. *Geophys. Res. Lett.* **25,** 3693–3696 (1998).
25. Blower, J. D. Factors controlling porosity-permeability relationships in magma. *Bull. Volcanol.* **63,** 497–504 (2001).
26. Klug, C. & Cashman, K. V. Permeability development in vesiculating magmas: implications for fragmentation. *Bull. Volcanol.* **58,** 87–100 (1996).
27. Klug, C., Cashman, K. V. & Bacon, C. R. Structure and physical characteristics of pumice from the climactic eruption of Mount Mazama (Crater Lake), Oregon. *Bull. Volcanol.* **64,** 486–501 (2002).
28. Gottsmann, J. & Dingwell, D. B. The thermal history of a spatter-fed lava flow: the 8-ka pantellerite flow of Mayor Island, New Zealand. *Bull. Volcanol.* **64,** 410–422 (2002).
29. Smith, J. V. Ductile-brittle transition structures in the basal shear zone of a rhyolite lava flow, eastern Australia. *J. Volcanol. Geotherm. Res.* **72,** 217–223 (1996).
30. Martel, C., Dingwell, D. B., Spieler, O., Pichavant, M. & Wilke, M. Experimental fragmentation of crystal- and vesicle-bearing melts. *Bull. Volcanol.* **63,** 398–405 (2001).

Acknowledgements We thank P. Papale and D. L. Sahagian for comments on the previous versions of the manuscript, and K. V. Cashman, A. Rust, and A. M. Jellinek for comments on earlier versions. This work was supported by the National Science Foundation and the Sloan Foundation.

Competing interests statement The authors declare that they have no competing financial interests.

Correspondence and requests for materials should be addressed to H.M.G. (hmg@seismo.berkeley.edu).

Language-tree divergence times support the Anatolian theory of Indo-European origin

Russell D. Gray & Quentin D. Atkinson

Department of Psychology, University of Auckland, Private Bag 92019, Auckland 1020, New Zealand

Languages, like genes, provide vital clues about human history[1,2]. The origin of the Indo-European language family is "the most intensively studied, yet still most recalcitrant, problem of historical linguistics"[3]. Numerous genetic studies of Indo-European origins have also produced inconclusive results[4,5,6]. Here we analyse linguistic data using computational methods derived from evolutionary biology. We test two theories of Indo-European origin: the 'Kurgan expansion' and the 'Anatolian farming' hypotheses. The Kurgan theory centres on possible archaeological evidence for an expansion into Europe and the Near East by Kurgan horsemen beginning in the sixth millennium BP[7,8]. In contrast, the Anatolian theory claims that Indo-European languages expanded with the spread of agriculture from Anatolia around 8,000–9,500 years BP[9]. In striking agreement with the Anatolian hypothesis, our analysis of a matrix of 87 languages with 2,449 lexical items produced an estimated age range for the initial Indo-European divergence of between 7,800 and 9,800 years BP. These results were robust to changes in coding procedures, calibration points, rooting of the trees and priors in the bayesian analysis.